ISSN 0036-0244, Russian Journal of Physical Chemistry A, 2023, Vol. 97, No. 13, pp. 3004–3012. © Pleiades Publishing, Ltd., 2023.

CHEMICAL KINETICS AND CATALYSIS

Synthesis of Highly-Active Cu_2O for Degradation of MO Dyes under Light and Non-light Conditions by Electrochemical Method

Xujie Xiao[a], Wenxin Zheng[a], Haoran Yin[a], Xu Li[a], and Chengfei Zhu[a,*]

[a]*College of Materials Science and Engineering, Nanjing Tech University, Nanjing, Jiangsu, 210009 China*

** e-mail: Njtechzhucf@163.com*

Received July 7, 2023; revised July 7, 2023; accepted July 21, 2023

Abstract—The growth of Cu_2O crystal planes was be controlled by adding surfactant to the NaCl solution in this manuscript. The structure and composition of the synthesized Cu_2O particles were characterized by X-ray diffraction (XRD), X-ray photoelectron spectroscopy (XPS), field emission scanning electron microscopy (FESEM), and specific surface area test method (BET). The photocatalytic activities were evaluated by degrading methyl orange (MO) solution under magnetic stirring. The results shown that the synthesized Cu_2O particle was spherical self-assembly structure when the surfactant was CTAB, and behaved higher degradation performance. Under dark conditions, the adsorption efficiency of 100 mg L^{-1} MO solution reached 67.08% in the first 1 min by 0.33 g L^{-1} CTAB-Cu_2O, and after 15 min, the adsorption degradation efficiency of MO had reached 99.17%. The maximum adsorption capacity of CTAB-Cu_2O was 297.28 mg g^{-1}. The adsorption kinetics obeyed pseudo-second-order kinetics and followed the Freundlich isotherm.

Keywords: cuprous oxide, electrochemical method, photocatalytic degradation, non-light conditions, surfactant

DOI: 10.1134/S0036024423130307

1. INTRODUCTION

With the development of industrialization, dye wastewater, as one of the hard-to-degrade industrial wastewaters, was becoming increasingly harmful to water bodies [1]. Semiconductor photocatalysis degradation was a process which semiconductors produce electron-hole pairs with strong redox properties, so that many dye macromolecules which were structurally stable in structure or even difficult to be decomposed by micro-organisms were converted into small molecules which were non-toxic, harmless and biodegradable [2]. Compared with other methods, the semiconductor photocatalysis method had the advantages of fast speed, complete degradation, low energy consumption, and no secondary pollution.

In addition to the most widely used TiO_2, some new photocatalysts with visible light response had been studied, such as simple oxides (Bi_2O_3, Cu_2O, ZnO, ZrO_2) [3, 4], sulfide (CdS, WS_2, SnS_2) [5], composite oxide (Bi_2WO_6) [6, 7], nitride (C_3N_4) [8, 9], and so on. Cuprous oxide (Cu_2O), an attractive typical p-type semiconductor, had a narrow bandgap of 2.17 eV. As one of the few semiconductor materials that could be excited by visible light, Cu_2O had strong electron–hole pair activity and exhibited good photocatalytic activity. Many researchers had prepared Cu_2O with different morphologies to increase the photocatalytic activity, such as nanowires, nanospheres, thin films, cubes and octahedrons, and so on [10]. Yang et al. [11] synthesized Cu_2O by a simple liquid-phase reduction method, the morphology of Cu_2O was adjusted by changing the preparation temperature, and the results showed that Cu_2O prepared at 60°C had the best effect to degrade MO solution, and the degradation efficiency reached 96.79% after 30 min of photocatalytic reaction. Prado-Chay et al. [12] synthesized Cu_2O through a simple chemical method, which had microspheres structure and exhibited high photocatalytic activity up to 76% during decolorization of MO. Tang et al. [13] reported that Cu_2O nanocubes of different sizes (20–400 nm) was prepared by a seed-mediated method. The results showed that Cu_2O with particle size of 30 nm exhibited high photocatalytic degradation activity for MO, and after 3 h of reaction, the degradation efficiency was close to 70%. Therefore, Cu_2O had potential application prospects in the fields of photocatalysis with visible light.

However, it could not be guaranteed that the entire process of the discharge and treatment of dye wastewater would be under visible light conditions. The research on the degradation performance of Cu_2O under non-light conditions had not been extensively explored.

Compared with other liquid-phase preparation methods, the electrochemical method had the advantages of simple equipment, low cost, easy control of process parameters and easy realization of controllable product morphology. However, there were still few reports on the electrochemical method of preparing Cu_2O by adding surfactants to control the morphology. At the same time, many researchers found that surfactants were often used to improve its performance of nanoparticles. Kim et al. [14] synthesized the Cu_2O by changing the addition amount of the surfactant polyvinylpyrrolidone (PVP) in the liquid phase. When the addition amount of PVP was 16 g, Cu_2O showed higher cycle performance in lithium-ion batteries. Lv et al. [15] adjusted the morphology of Cu_2O by adding Sodium dodecyl sulfate (SDS) additives in solution. The prepared Cu_2O nanocages had excellent activity and catalytic performance. Bae et al. [16] prepared polygonal stacked Cu_2O by simply controlling the concentration of cetyltrimethylammonium bromide (CTAB) and improving the Benedict reaction, the synthesized pointed structure had a higher battery capacity than the round structure.

In this work, in order to fully optimize the performance of Cu_2O photocatalytic degradation of MO dye wastewater, the different Cu_2O structures were synthesized by electrochemical anodic oxidation method in facile NaCl solution, and cetyltrimethylammonium bromide (CTAB), sodium dodecyl sulfate (SDS), polyethylene glycol (PEG), and polyvinyl pyrrolidone (PVP) were used as surfactants.

2. EXPERIMENTAL

2.1. Synthesis of Cu_2O

17 wt % NaCl (AR, 99.5%, Sinopharm Chemical Reagent Co., Ltd.) and 0.3 wt % D-calcium gluconate monohydrate ($D\text{-}C_{12}H_{22}O_{14}Ca\cdot H_2O$, AR, 99%, Macklin) were dissolved in deionized water (18.3 MΩ). 20 wt % NaOH was slowly dripped to the solution to adjust the pH value to 11.5. Then 0.25 wt % different surfactants, CTAB, SDS, PEG, and PVP were added into the electrolyte. Pure Cu plate ($50 \times 25 \times 2$ mm^3) was used as the anode, graphite as the cathode. And a Direct current power supply was used to provide a constant current of 0.4 A. During the reaction, the 35°C temperature was controlled by a constant temperature water bath. The solution reaction was 60 min, then the product were washed, filtered, and dried to obtain a powder sample.

2.2. Characterization of Structure and Morphology

The structure of synthesized Cu_2O particles were tested by the ARL XTRA powder X-ray diffractometer with CuK_α radiation (XRD). The X-ray photoelectron spectroscopy (XPS) was performed on Perkin Elmer PHI-1600 ESCA spectrometer (MgK_α) to determine the valence states of the constituent elements. Field-emission scanning microscopy (FESEM) was performed to analyze the morphology of Cu_2O particles with a JSM-7600F instrument operating at 15 kV, and thin gold films were sprayed on the samples before the characterization. The surface area and adsorption performance of the Cu_2O particles were analyzed by BET specific surface area test method.

2.3. Photocatalytic Degradation

The photocatalytic activity of the synthesized Cu_2O particles was evaluated by degrading MO (MO, 96%, Macklin) under magnetic stirring in photocatalytic reactor. The irradiation of visible light was simulated by xenon lamp (light power 100 mW cm^{-2}), 1 g L^{-1} of the Cu_2O photocatalyst was dispersed in 20 mg L^{-1} MO solution. The temperature was controlled to be constant for 25°C through a double channel glass tube water bath. During the photocatalytic experiment, the xenon lamp was turned off for 10 min under magnetic stirring to ensure that the adsorption equilibrium between the photocatalyst and the MO. Then, the solution was exposed to light irradiation under magnetic stirring for a set time. The concentration of MO was evaluated at different time by measuring its UV–Vis characteristic absorption peak at 464 nm. Under this wavelength, the absorbance of MO could be accurately analyzed to obtain the photocatalytic degradation rate. UV–Vis absorption spectra were acquired using an AOE A590 spectrophotometer (Shanghai Ao Arts Co., Ltd.). Ultraviolet-visible diffuse reflectance spectroscopy (UV–Vis DRS) of Cu_2O samples was measured by UV-visible diffuse reflectance spectrometer UV3600i plus.

Three Cu_2O samples (Cu_2O, SDS-Cu_2O, CTAB-Cu_2O) were selected to analyze the degradation process under dark reaction conditions. The addition amount of Cu_2O was reduced to 0.33 g L^{-1}, and the concentration of the MO solution was increased to 100 mg L^{-1}. The experimental procedures were similar to the above.

3. RESULTS AND DISCUSSION

3.1. Morphology and Composition Characterization

Figure 1 was the XRD patterns of Cu_2O prepared in electrolytes with different surfactants. All the diffraction peaks were indexed to the phase of Cu_2O (JCPDS no. 78-2076). The peaks at $2\theta = 29.9°$, 36.5°, 42.2,° 61.4°, and 73.81° could be indexed to the (110), (111), (200), (220), and (311) reflection peaks, which indicated that all synthesized particles were cubic phase Cu_2O. When the surfactant was CTAB, the peak intensity of Cu_2O prepared was lower and the peak width

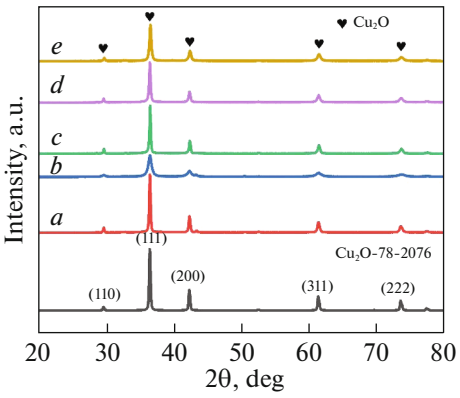

Fig. 1. X-ray diffraction pattern of the Cu_2O prepared in electrolytes with different surfactants: (*a*) Cu_2O, (*b*) CTAB-Cu_2O, (*c*) SDS-Cu_2O, (*d*) PEG-Cu_2O, (*e*) PVP-Cu_2O.

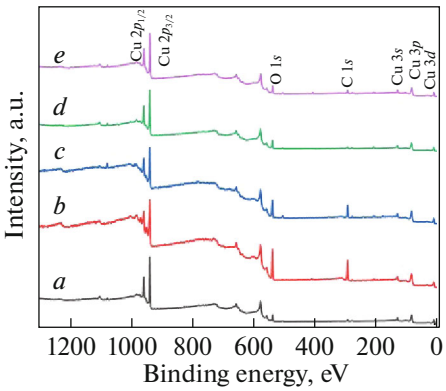

Fig. 2. XPS full spectrum of Cu_2O prepared in electrolytes with different surfactants: (*a*) Cu_2O, (*b*) CTAB-Cu_2O, (*c*) SDS-Cu_2O, (*d*) PEG-Cu_2O, (*e*) PVP-Cu_2O.

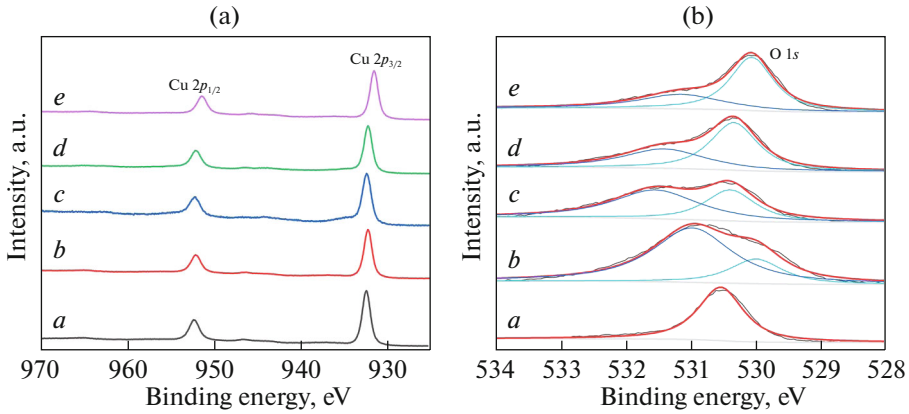

Fig. 3. Cu and O elemental analysis spectra of Cu_2O: (*a*) Cu_2O, (*b*) CTAB-Cu_2O, (*c*) SDS-Cu_2O, (*d*) PEG-Cu_2O, (*e*) PVP-Cu_2O.

was wider, which showed that the Cu_2O had low crystallinity.

The XPS full-range survey scan and the Cu and O elemental analysis spectra of the Cu_2O powder samples were shown in Figs. 2, 3. The XPS scan had confirmed the presence of Cu and O, and there was no foreign material present in the samples. In the XPS spectrum of CTAB-Cu_2O, the peak intensity of O 1*s* was higher. Figure 3a clearly displayed that Cu 2*p* had two sub-energy levels, Cu $2p_{1/2}$ and Cu $2p_{3/2}$, and their characteristic peaks correspond to binding energies of 951.4–952.3 and 931.5–932.4 eV, respectively. These were roughly consistent with the peak positions of Cu $2p_{1/2}$ and Cu $2p_{3/2}$ in [17, 18]. The XPS patterns collected confirmed that all the samples were indeed Cu_2O.

The O 1*s* peak could be divided into lattice oxygen (O_{latt}) and adsorbed oxygen (O_{ads}) according to the binding energy, which were located at 529.5–530.5 V and 531–531.5 eV, respectively. It could be seen that CTAB-Cu_2O had the strongest O_{ads} peak, which meant that there was the most O_{ads} in CTAB-Cu_2O structure [19].

Figure 4 displayed the FESEM images of Cu_2O. When no additive added, the morphology of Cu_2O was regular octahedra with holes. After adding the surfactants CTAB, SDS, PEG, and PVP in the electrolyte, different Cu_2O structures, spherical self-assembly structure, regular octahedra, octahedra with narrow edges, and agglomerated octahedra with small particle size, were synthesized. It could be seen that in addition to CTAB, the Cu_2O structures with the other three surfactants maintained the octahedral, but the particle size and surface etched phenomenon were slightly different.

According to the formation mechanism of Cu_2O combined with anodic oxidation, the crystallization process of Cu_2O was divided into three steps: nucle-

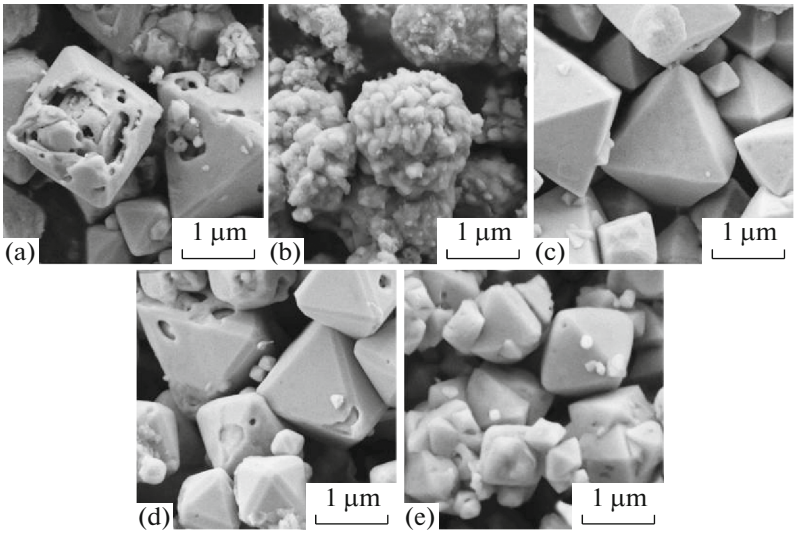

Fig. 4. FESEM images of the sample prepared by anodizing method: (a) Cu_2O, (b) CTAB-Cu_2O, (c) SDS-Cu_2O, (d) PEG-Cu_2O, and (e) PVP-Cu_2O.

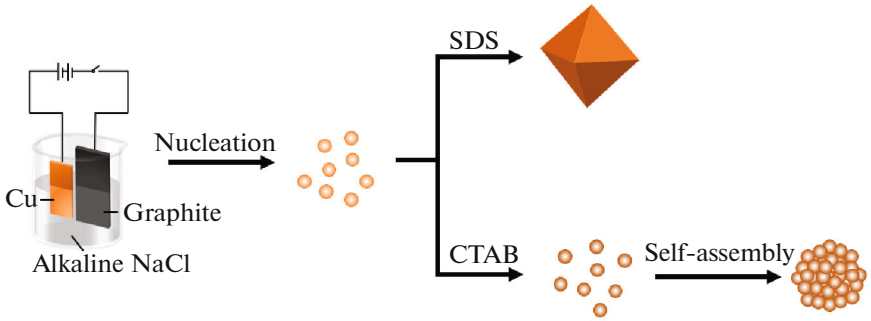

Fig. 5. Schematic diagram describing the nucleation and growth of particles as well as secondary structures of Cu_2O when SDS and CTAB were added.

ation, growth and dissolution. The pH value of the solution deeply affected the dissolution of the Cu_2O surface. When the solution was alkaline, more OH^- reacted with generated Cu_2O to dissolve into $Cu(OH)_2^-$. So when the pH value was 11.5, the etched octahedral appeared [20].

The preferential adsorption of surfactants on the crystal plane determined the crystal habits of electrochemically grown Cu_2O crystals. The preferential adsorption of SDS, PEG, and PVP on the (111) crystal plane played a role in protecting the crystal plane [21] during the dissolution process, therefore Cu_2O was a regular octahedra. The average size of the Cu_2O became smaller as the PVP was added to the solution, because the tight capping effect of PVP on the octahedra surfaces could block the further growth of octahedra [22].

CTAB mainly affected the growth process, which acted as structure-directing agent absorbed on the surface of the nanoparticles to prevent the growth and influence the aggregation process of the nano-particles. At slightly lower concentrations, called the critical micelle concentration (CMC1), the individual CTAB molecules formed small, spherical aggregates (micelles) [23]. The surface modified nanoparticles self-assemble into Cu_2O microspheres with the extension of the reaction time (Fig. 5). As a result, the spherical self-assembly structure was formed after the reaction finished [24].

From the nitrogen adsorption-desorption curves of Cu_2O in Fig. 6, the specific surface area (SSA) of Cu_2O could be calculated. The SSA values were calculated as 3.249, 3.809, 1.968, 2.258, and 3.407 $m^2\ g^{-1}$ for Cu_2O, CTAB-Cu_2O, SDS-Cu_2O, PEG-Cu_2O, and PVP-Cu_2O, respectively. The CTAB-Cu_2O had the

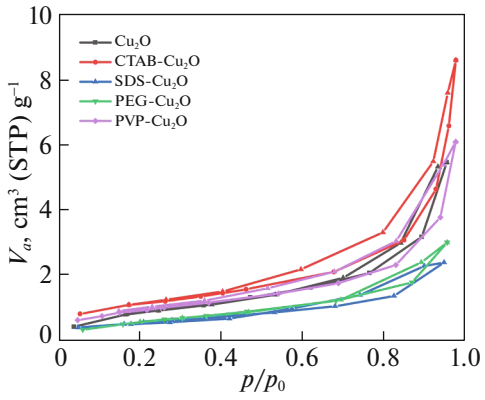

Fig. 6. Nitrogen adsorption-desorption isotherm of Cu_2O sample.

largest specific surface area, and this result was consistent with the FESEM image in Fig. 4.

3.2. Photocatalytic Performance

As shown in Fig. 7a, the Cu_2O particles in the MO solution had a certain absorption peak in the visible light range. Thus, the Cu_2O particles could interact with the negatively charged MO for degradation. The band gap of the sample could be calculated according to the Tauc formula [25]:

$$\alpha h\nu^2 = A(h\nu - E_g). \quad (1)$$

Among them, α was the absorption coefficient, h was the Planck constant (6.63×10^{-34}), ν was the optical frequency, A was the constant, and E_g was the band gap energy.

According to the formula conversion, $(\alpha h\nu)^2$ was plotted against $h\nu$ (Fig. 7b). By extrapolating the linear part of the curve $(\alpha h\nu)^2 = 0$, the values of Cu_2O, CTAB-Cu_2O, SDS-Cu_2O, PEG-Cu_2O, and PVP-Cu_2O were 1.862, 1.669, 1.867, 1.881, and 1.864 eV, respectively. The prepared CTAB-Cu_2O particles had a narrow bandgap, illustrated that the number of photogenerated electrons and holes increased [26].

The UV–Vis absorption spectra of Cu_2O particles prepared with different surfactants in the electrolyte for MO degradation under visible light irradiation was shown in Fig. 8. All the Cu_2O samples displayed excellent light-harvesting capabilities in the wavelength range 464 nm due to the low bandgap of Cu_2O. The characteristic absorption peak of MO at 464 nm gradually decreased and disappeared with the extension of UV time. Which indicated that the degradation of MO was complete.

The efficiency curves (degradation efficiency versus time) and kinetics curves ($\ln(C_0/C)$ versus time) of the Cu_2O particles prepared from electrolytes with different surfactants for MO degradation under visible light irradiation as shown in Fig. 9. The degradation efficiency was calculated by the following formula [27]:

$$\eta = (C_0 - C)/C_0 \times 100\% = (A_0 - A)/A_0 \times 100\%. \quad (2)$$

Among them, C_0 was the initial concentration of MO, C was the concentration after the illumination time t, A_0 was the initial absorbance of MO, and A was the absorbance after the illumination time t.

According to Fig. 9a, after plotting $\ln(C_0/C)$ versus time and fitting it, the logarithm of the concentration ratio shown a linear relationship (Fig. 9b). Its characteristic equation was:

$$\ln(C_0/C) = kt. \quad (3)$$

Among them, k was the first-order reaction rate constant.

So the photocatalytic degradation satisfied the Langmuir–Hinshelwood kinetic equation, and the photocatalytic oxidation reaction conforms to the first-order reaction kinetic characteristics [28].

After the 10 min dark reaction, the MO solution had been partially adsorption degraded by Cu_2O, the

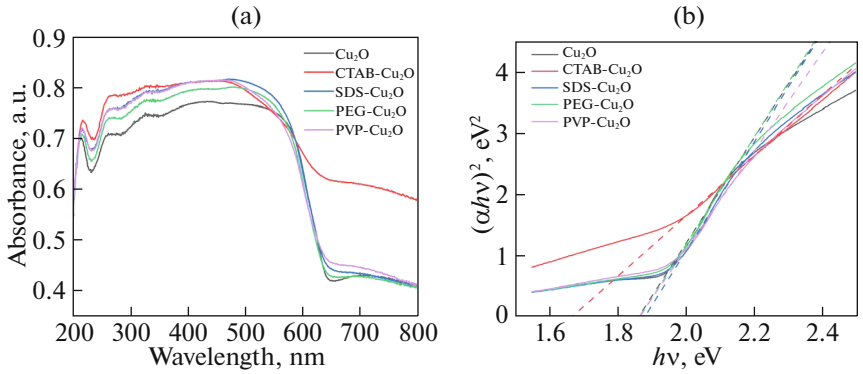

Fig. 7. (a) DRS diagram of Cu_2O; (b) $(\alpha h\nu)^2$–$h\nu$ relationship curve.

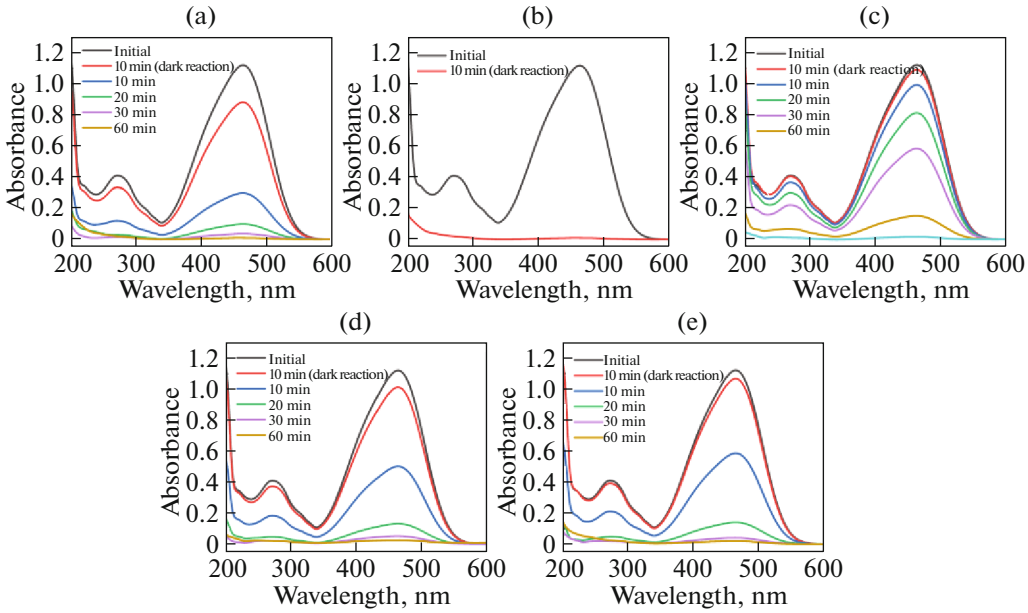

Fig. 8. Photocatalytic degradation of MO solution by Cu_2O catalyst: (a) Cu_2O, (b) CTAB-Cu_2O, (c) SDS-Cu_2O, (d) PEG-Cu_2O, and (e) PVP-Cu_2O.

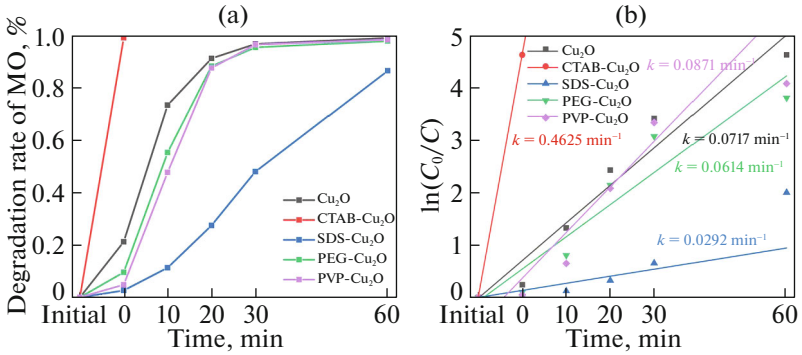

Fig. 9. Analysis of Cu_2O catalyst's photocatalytic degradation process of MO solution: (a) degradation efficiency and (b) kinetic curve.

degradation efficiencies of Cu_2O to MO solution were 21.21, 99.01, 2.67, 9.53, and 4.81%, respectively. After 60 min of photocatalytic degradation, the degradation efficiencies of Cu_2O, CTAB-Cu_2O, SDS-Cu_2O, PEG-Cu_2O, and PVP-Cu_2O to MO solution were 98.31, 99.01, 86.45, 97.72, and 98.89%, respectively. The k values of MO solution were: 0.0717, 0.4625, 0.0292, 0.0614, and 0.0871 min^{-1}, respectively. They all had obvious degradation effects on MO solutions.

It presented that Cu_2O had the adsorption and degradation effect on MO solution, and the effect of CTAB-Cu_2O was extremely excellent. It because that CTAB-Cu_2O had the higher specific surface area and there was the largest amount of photogenerated electrons, holes in CTAB-Cu_2O structure.

In the previous study, it was found that the efficiency of CTAB-Cu_2O to degrade MO solution was 99.01% in 10 min dark reaction. Therefore, in the next experiment, the degradation of MO by Cu_2O was studied specifically under non-light conditions. Figure 10 was the analysis of the degradation process of 0.33 g L^{-1} Cu_2O, CTAB-Cu_2O, and SDS-Cu_2O on the 100 mg L^{-1} MO solution under non-light conditions. It could be clearly seen that the characteristic absorption peak of MO at 464 nm gradually decreased. The degradation efficiency of Cu_2O after degrading the MO solution for 600 min was 69.02%, and SDS-Cu_2O was only 58.39%. But after 15 min, the characteristic absorption peaks of MO in the solution containing CTAB-Cu_2O almost disappeared, indicating that the degradation of

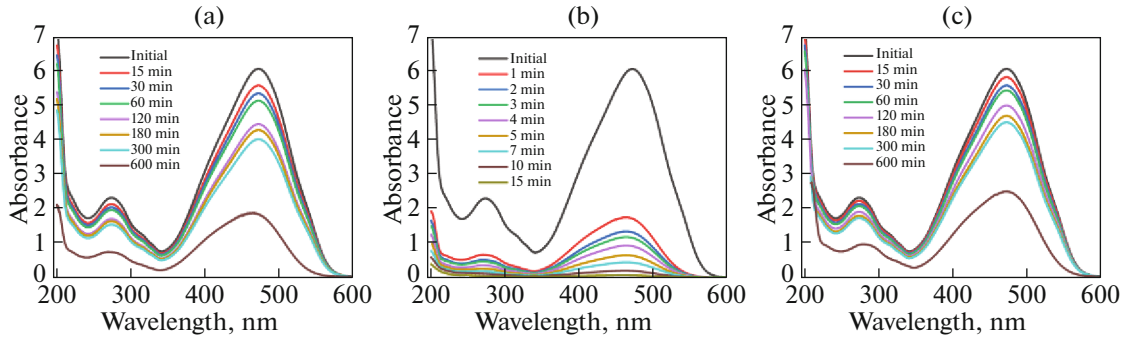

Fig. 10. Analysis of the degradation process of Cu_2O on MO solution under no-light conditions: (a) Cu_2O, (b) CTAB-Cu_2O, and (c) SDS-Cu_2O.

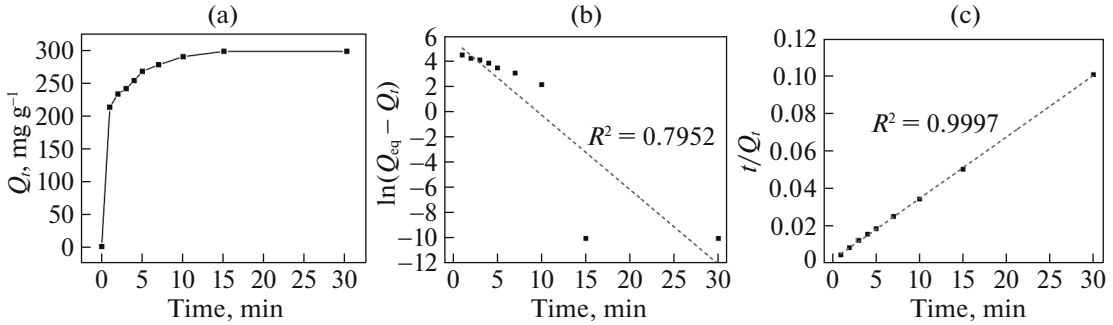

Fig. 11. Kinetic model of CTAB-Cu_2O degrade MO solution under non-light conditions: (a) time-dependent adsorption amount of CTAB-Cu_2O, (b) the pseudo-first kinetic model, (c) the pseudo-second-order kinetic model.

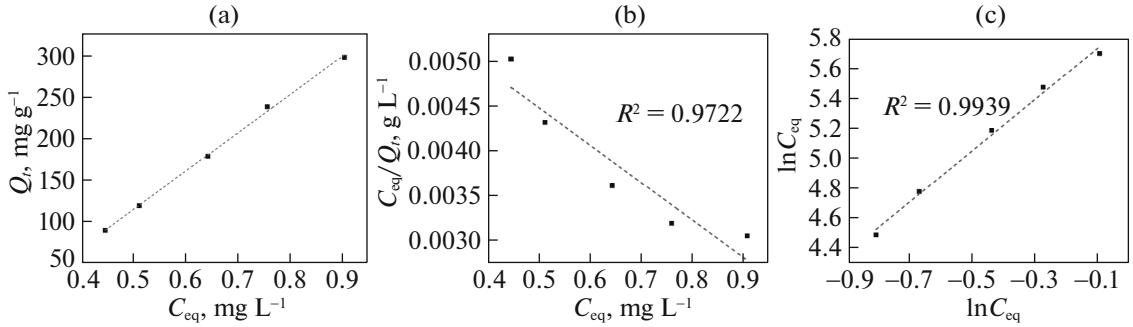

Fig. 12. Isotherm model of CTAB-Cu_2O degrade MO solution under non-light conditions: (a) adsorption isotherm for MO on CTAB-Cu_2O, (b) plots of C_{eq}/Q_{eq} against C_{eq} based on isotherm Langmuir model, (c) plots of ln Q_{eq} against ln C_{eq} based on isotherm Freundlich model.

MO was complete. Which showed that the CTAB-Cu_2O had an extremely remarkable degradation performance for MO solution under non-light conditions.

Figures 11, 12 displayed the degradation kinetics model and isotherm model analysis of CTAB-Cu_2O to degrade MO solution under non-light conditions. The adsorption capacity could be calculated by the concentration-absorbance curve, the calculation formula of adsorption capacity [29]:

$$Q_t = \frac{V(C_0 - C_t)}{m}. \quad (4)$$

In the formula, Q_t (mg g^{-1}) is equilibrium adsorption capacity; C_0, C_t (mg L^{-1}) is the initial concentration of dye and the concentration at adsorption equilibrium; V (L) is dye volume.

Figure 11a was the curve of the adsorption capacity of CTAB-Cu_2O to degrade MO over time. After 1 min of adsorption, the degradation efficiency of the adsor-

bent to degrade MO solution reached 67.08%, and the adsorption capacity was 212.21 mg g^{-1}. After 15 min, the degradation efficiency reached 99.23%. At this time, the adsorption capacity of CTAB-Cu_2O on MO reached 297.28 mg g^{-1}. It because that there was the higher specific surface area and the largest amount of O_{ads} in CTAB-Cu_2O structure.

The adsorption kinetics was closely related to the contact time. To understand the characteristics of the adsorption process of MO on different Cu_2O samples, the two traditional adsorption models, namely the pseudo-first and the pseudo-second-order kinetic models, were used to describe the adsorption process.

The pseudo-first-order equation [30] was expressed as:

$$\ln(Q_{eq} - Q_t) = tK_1. \quad (5)$$

The linear form of pseudo-second-order kinetics equation [31] could be described as follows:

$$\frac{t}{Q_t} = \frac{t}{Q_{eq}} + \frac{1}{K_2 Q_{eq}^2}. \quad (6)$$

In the formula, Q_{eq} (mg g^{-1}) is the adsorption amounts at the equilibrium; Q_t (mg g^{-1}) is the adsorption amounts at arbitrary time t; K_1 (min^{-1}), K_2 (g mg^{-1} min^{-1}) are rate constants.

Figures 11b, 11c were the graphs obtained by linear fitting of the quasi-first-order kinetic equation and the quasi-second-order kinetic equation on the experimental results. In contrast, the R^2 values of CTAB-Cu_2O for the pseudo-second-order kinetic model was close to 1 ($R^2 = 0.9997$), thus confirming that the adsorption behavior followed a pseudo-second-order kinetic model. This reflected that the adsorption process was electrostatic adsorption, and the kinetic constant K_2 was 5.39×10^{-3} g mg^{-1} min^{-1}.

To describe how the adsorbents distribute along the liquid/adsorbent interface, two well-known isotherm models, namely the Langmuir and Freundlich models, were employed to analyze the experimental data [32, 33].

The linear form of Langmuir isotherm equation could be expressed as:

$$\frac{C_{eq}}{Q_{eq}} = \frac{1}{K_L Q_m} + \frac{C_{eq}}{Q_m}. \quad (7)$$

The linear form of the Freundlich isotherm equation can be represented as:

$$\ln Q_{eq} = \ln K_F + b_F \ln C_{eq}, \quad (8)$$

where C_{eq} (mg/L) and Q_{eq} (mg/g) were the equilibrium concentration and adsorption capacity of samples, respectively; b_F was a constant depicting the adsorption intensity, K_F was the Freundlich constant, and K_L was the Langmuir constant.

Plotted of C_{eq}/Q_{eq} against C_{eq} based on Langmuir isotherm model and those of $\ln Q_{eq}$ against $\ln C_{eq}$ based on Freundlich isotherm model were shown in Figs. 12b, 12c.

As shown in Figs. 12b, 12c, good linear relations were obtained, indicating that the process of CTAB-Cu_2O degraded MO solution fit both the Langmuir and Freundlich models. The values of R^2 for Freundlich isotherm model ($R^2 = 0.9939$) was higher than that for Langmuir isotherm model ($R^2 = 0.9722$), indicating that the Langmuir isotherm model was more suitable for describing the adsorption. Which showed that the adsorption reaction was multi-molecular layer adsorption, and the adsorption sites on the adsorbent were not uniformly distributed. The rate constant $K_F = 368.04$, this value could be regarded as the adsorption capacity per unit concentration.

4. CONCLUSIONS

In this study, Cu_2O crystal was synthesized with systematic morphology evolution from octahedral to self-assembly spherical. Their structures had been extensively analyzed. The spherical self-assembly structure was found that CTAB which acted as structure-directing agent absorbed on the surface of the nanoparticles and influenced the growth and aggregation process of the nano-particles. CTAB-Cu_2O exhibited exceptionally good photocatalytic activity. Under dark conditions, when 1 g L^{-1} CTAB-Cu_2O degraded 20 mg L^{-1} MO solution, the degradation efficiency reached 99.01% after 10 min, the efficiency of 0.33 g L^{-1} CTAB-Cu_2O to degrade 100 mg L^{-1} MO solution reached 67.08% in the first 1 min. After 15 min, the degradation efficiency reached 99.17%. And the maximum adsorption capacity was 297.28 mg g^{-1}. The adsorption kinetics obeyed pseudo-second-order kinetics following the Freundlich isotherm.

AUTHOR CONTRIBUTIONS

X.X. and C.Z. conceived and supervised the project. X.X. prepared the samples and performed the measurements and characterizations. X.X. and C.Z. co-wrote this paper. All the authors discussed the results and commented on the manuscript.

FUNDING

This study was supported by the National Natural Science Foundation of China (grant no. 21203095), the Jiangsu National Synergetic Innovation Center for Advanced Materials (SICAM) and the Priority Academic Program Development of Jiangsu Higher Education Institutions.

CONFLICT OF INTEREST

The authors declare that they have no conflicts of interest.

REFERENCES

1. A. Tkaczyk, K. Mitrowska, and A. Posyniak, Sci. Total Environ. **717**, 137222 (2020). https://doi.org/10.1016/j.scitotenv.2020.137222
2. A. Singh and S. Kumar, Appl. Phys. A **127** (11) (2021). https://doi.org/10.1007/s00339-021-04993-w
3. W. He, Y. Sun, G. Jiang, H. Huang, X. Zhang, and F. Dong, Appl. Catal. B **232**, 340 (2018). https://doi.org/10.1016/j.apcatb.2018.03.047
4. Z. Zeng, Y. Yan, J. Chen, P. Zan, Q. Tian, and P. Chen, Adv. Funct. Mater. **29** (2) (2019). https://doi.org/10.1002/adfm.201806500
5. C. Byrne, G. Subramanian, and S. C. Pillai, J. Environ. Chem. Eng. **6**, 3531 (2018). https://doi.org/10.1016/j.jece.2017.07.080
6. Z. Gou, J. Dai, and J. Bai, Int. J. Electrochem. Sci. **15**, 10684 (2020). https://doi.org/10.20964/2020.11.68
7. H. Yi, M. Jiang, D. Huang, G. Zeng, C. Lai, L. Qin, C. Zhou, B. Li, X. Liu, M. Cheng, W. Xue, and P. Xu, J. Taiwan Inst. Chem. Eng. **93**, 184 (2018). https://doi.org/10.1016/j.jtice.2018.06.037
8. C. Liu, Y. Zhang, F. Dong, A. H. Reshak, L. Ye, N. Pinna, C. Zeng, T. Zhang, and H. Huang, Appl. Catal. B **203**, 465 (2017). https://doi.org/10.1016/j.apcatb.2016.10.002
9. T. Xiong, W. Cen, Y. Zhang, and F. Dong, ACS Catal. **6**, 2462 (2016). https://doi.org/10.1021/acscatal.5b02922
10. S. Yu, Y. Jiang, Y. Sun, F. Gao, W. Zou, H. Liao, and L. Dong, Appl. Catal. B **284,** 119743 (2021). https://doi.org/10.1016/j.apcatb.2020.119743
11. X. Yang, S. Zhang, L. Zhang, B. Zhang, and T. Ren, RCS Adv. **9**, 36831 (2019). https://doi.org/10.1039/c9ra07255a
12. D. A. Prado-Chay, M. A. Cortes-Jacome, C. Angeles-Chavez, R. Oviedo-Roa, J. M. Martinez-Magadan, C. Zuriaga-Monroy, I. J. Hernandez-Hernandez, P. R. Mayoral, D. R. Gomora-Herrera, and J. A. Toledo-Antonio, Top. Catal. **63**, 586 (2020). https://doi.org/10.1007/s11244-020-01256-5
13. Y. Tang, Y. Xu, C. Qi, X. Li, E. Xing, F. Wang, Z. Kan, C. Wang, J. Tang, G. Zheng, K. Zhang, X. Wang, C. Li, and K. Yang, J. Nanosci. Nanotechnol. **18**, 8282 (2018). https://doi.org/10.1166/jnn.2018.15879
14. E.-S. Kim, M.-C. Kim, S.-H. Moon, Y.-K. Shin, J.-E. Lee, S. Choi, and K.-W. Park, J. Alloys Compd. **794**, 84 (2019). https://doi.org/10.1016/j.jallcom.2019.04.225
15. T.-T. Lv, H.-X. Wang, X.-B. Ren, L.-C. Wang, R.-M. Ding, J.-P. Cao, and B.-L. Lv, CrystEngComm **22**, 8214 (2020). https://doi.org/10.1039/d0ce01418d
16. J. Bae, H. Han, Y. Kim, H. Ahn, M. Kim, and W. B. Kim, J. Phys. Chem. Solids **150**, 109849 (2021). https://doi.org/10.1016/j.jpcs.2020.109849
17. J. Ghijsen, L. H. Tjeng, J. Vanelp, H. Eskes, J. Westerink, G. A. Sawatzky, and M. T. Czyzyk, Phys. Rev. B **38**, 11322 (1988). https://doi.org/10.1103/PhysRevB.38.11322
18. S. Poulston, P. M. Parlett, P. Stone, and M. Bowker, Surf. Interface Anal. **24**, 811 (1996). https://doi.org/10.1002/(sici)1096-9918(199611)24:12<811::Aid-sia191>3.0.Co,2-z
19. C. Cao, H. Yang, J. Xiao, X. Yang, B. Ren, L. Xu, G. Liu, and X. Li, Fuel **305**, 121446 (2021). https://doi.org/10.1016/j.fuel.2021.121446
20. D. P. Singh, N. R. Neti, A. S. K. Sinha, and O. N. Srivastava, J. Phys. Chem. C **111**, 1638 (2007).
21. M. J. Siegfried and K. S. Choi, Adv. Mater. **16**, 1743 (2004). https://doi.org/10.1002/adma.200400177
22. Z. Xu, X. Yi, X. Fen, X. H. Liu, and X. Di, Inorg. Chem. Commun. **6**, 1390 (2003). https://doi.org/10.1016/j.inoche.2003.09.002
23. N. K. Raman, M. T. Anderson, and C. J. Brinker, Chem. Mater. **8**, 1682 (1996). https://doi.org/10.1021/cm960138+
24. X.-Y. Gong, Y.-P. Gao, L.-B. Wang, and P.-F. Guo, Nano **8**, 1350047 (2013). https://doi.org/10.1142/s1793292013500471
25. R. Lopez and R. Gomez, J. Sol-Gel Sci. Technol. **61**, 1 (2012). https://doi.org/10.1007/s10971-011-2582-9
26. Y. Y. Tang, Y. L. Xu, C. Y. Qi, X. Y. Li, E. M. Xing, F. Wang, Z. G. Kan, C. L. Wang, J. Y. Tang, G. L. Zheng, K. Zhang, X. H. Wang, C. L. Li, and K. Yang, J. Nanosci. Nanotechnol. **18**, 8282 (2018).
27. B. Bharti, S. Kumar, H.-N. Lee, and R. Kumar, Sci. Rep. **6** (2016). https://doi.org/10.1038/srep32355
28. S. Chakrabarti and B. K. Dutta, J. Hazard. Mater. **112**, 269 (2004). https://doi.org/10.1016/j.jhazmat.2004.05.013
29. J. Liu, Z. Gao, H. Han, D. Wu, F. Xu, H. Wang, and K. Jiang, Chem. Eng. J. **185**, 151 (2012). https://doi.org/10.1016/j.cej.2012.01.064
30. Y. S. Ho and G. McKay, Chem. Eng. J. **70**, 115 (1998). https://doi.org/10.1016/s0923-0467(98)00076-1
31. Y. S. Ho and G. McKay, Process Safety Environ. Prot. **76** (B4), 332 (1998). https://doi.org/10.1205/095758298529696
32. Y. Xu, P. Liu, Y. Cao, Y. Sun, and G. Zhang, Bull. Korean Chem. Soc. **37**, 1114 (2016). https://doi.org/10.1002/bkcs.10834
33. W. C. J. Ho, Q. Tay, H. Qi, Z. Huang, J. Li, and Z. Chen, Molecules **22**, 677 (2017). https://doi.org/10.3390/molecules22040677